netism, J. Jacobs, Ed. (Academic Press, Orlando, FL, 1987), vol. 2, p. 306.
3. Reviewed in P. Dyal *et al.*, *Rev. Geophys. Space Phys.* **12**, 568 (1974).
4. S. M. Cisowski *et al.*, *J. Geophys. Res. Suppl.* **88**, A691 (1983).
5. P. J. Coleman *et al.*, *Proc. Lunar Planet. Sci. Conf.* **3**, 2271 (1972).
6. K. A. Anderson *et al.*, *Space Sci. Instrum.* **1**, 439 (1975). R. P. Lin, *Phys. Earth Planet. Int.* **20**, 271 (1979).
7. K. A. Anderson and D. E. Wilhelms, *Earth Planet. Sci. Lett.* **46**, 107 (1979).
8. R. P. Lin, K. A. Anderson, L. L. Hood, *Icarus* **74**, 529 (1988).
9. D. E. Wilhelms, in *Geology of the Terrestrial Planets*, *NASA SP–469* (NASA, Washington, DC, 1984), p. 107.
10. K. A. Anderson *et al.*, *Earth Planet. Sci. Lett.* **34**, 141 (1977).
11. L. L. Hood, P. J. Coleman, Jr., D. E. Wilhelms, *Science*, **205**, 53 (1979).
12. There is some evidence that the virtual geomagnetic poles of these regions (the direction of the magnetic south pole of the moon-centered dipole that accounts for the observed crustal magnetic field) cluster around three axes. Changes in the global dipole orientation may have been caused by dynamo field reversals and reorientation of the moon's spin axis by giant impacts, although this interpretation is controversial [S. K. Runcorn, *Proc. Lunar Planet. Sci. Conf.* **11**, 1867 (1980); *Phys. Earth Planet. Int.* **29**, 135 (1982); L. L. Hood, *Proc. Lunar Planet. Sci. Conf.* **12**, 817 (1981)].
13. M. H. Acuña *et al.*, *Science* **279**, 1676 (1998).
14. M. H. Acuña *et al.*, *J. Geophys. Res.* **97**, 7799 (1992).
15. The ER and experiment electronics are mounted on a 2.5-m boom that was deployed shortly after launch. The MAG sensor, which is separated from the ER electronics by a 1.2-m deployable boom, is a wide-range (up to 65,536 nT), low-noise (6 pT root mean square), high-sensitivity (as low as 2 pT) triaxial fluxgate magnetometer that measures magnetic fields from dc up to a sample rate of 18 Hz. The ER sensor consists of a symmetric hemispherical electrostatic analyzer that focuses incoming electrons onto an imaging detector that provides fine (~1.4°) angular resolution in the plane of its 360° by 14° disk-shaped field of view (FOV). The analyzer is stepped in voltage through the entire energy range (~10 to 20 keV) 32 times per spacecraft spin, and the ER is oriented so that its FOV covers the full sky (4π sr) every half spin (~2.5 s). Thus, the full three-dimensional distribution of electrons can be obtained every half spin, but because of telemetry rate limitations it is only transmitted once every 16 spins (80 s, corresponding to ~120 km of spacecraft motion). High temporal or spatial resolution mapping (2.5 s or ~4 km) is provided in two energy channels by computing pitch angle bins with the magnetic field direction measured by the MAG, sorting the electron counts into the bins on board the spacecraft, and sending only the one-dimensional pitch angle distribution to the ground.
16. If the field varies spatially and the fractional change in the field is small over the distance traveled by the electron in one gyration, then the adiabatic approximation holds: $(\sin^2\alpha)/|\mathbf{B}|$ = constant. For an isotropic pitch angle distribution, R depends only on the solid angle subtended by α_c, and we obtain $|\mathbf{B}_s| = |\mathbf{B}_h|/(1 - R^2)$, where $|\mathbf{B}_s|$ and $|\mathbf{B}_h|$ are the magnetic field strengths at the surface and the spacecraft, respectively. Hence, R provides a monotonic but nonlinear measure of the surface field strength, which is the vector sum of $\mathbf{B}_h$ and the crustal remanent field, $\mathbf{B}_r$. Coulomb scattering at the surface generates a small background of upward traveling electrons, resulting in $R \sim 0.05$ even in the absence of magnetic reflections. Surface magnetic fields a few times stronger than the field measured at the spacecraft can increase the reflection coefficient to nearly unity. For typical field strengths at the moon's location in the geomagnetic tail, R is a useful measure of crustal magnetic fields in the ~0.1 to 10 nT range. The dynamic range of ER magnetometry can be extended to $\sim 10^{-2}$ to 10^4 nT by measuring α_c directly from the pitch angle distribution.
17. L. Hood and Z. Huang, *J. Geophys. Res.* **96**, 9837 (1991).
18. Hilly terrain antipodal to the Imbrium and Orientale basins is thought to be produced by the focusing of seismic waves generated by those impacts [P. H. Schultz and D. E. Gault, *Moon* **12**, 159 (1975)].
19. L. L. Hood and A. Vickery, *J. Geophys. Res.* **89**, C211 (1984).
20. M. Fuller *et al.*, *Moon* **9**, 57 (1974).
21. The early sun's magnetic field may have been several orders of magnitude stronger than the present-day field, but by ~4 Ga, its field was probably far too weak to account for $\sim 10^{-5}$-T fields at the Earth's orbital distance. Such strong fields are also incompatible with terrestrial paleomagnetic data. For a review, see R. T. Merrill, M. W. McElhinny, P. L. McFadden, in *The Magnetic Field of the Earth: Paleomagnetism, the Core, and the Deep Mantle*, R. Dmowska and J. R. Holton, Eds. (International Geophysics Series, Academic Press, San Diego, CA, 1996), vol. 63, pp. 217–247.
22. L. Hood *et al.*, *J. Geophys. Res.* (*Suppl.*) **92**, E396 (1981).
23. L. Hood and G. Schubert, *Science* **208**, 49 (1980).
24. P. Dyal *et al.*, *Proc. Lunar Planet. Sci. Conf.* **5**, 3059 (1974).
25. B. E. Goldstein, *J. Geophys. Res.* **79**, 23 (1974).
26. Reviewed in C. P. Sonett, *Rev. Geophys. Space Phys.* **20**, 411 (1982).
27. D. S. Colburn, R. G. Currie, J. D. Mihalov, C. P. Sonett, *Science* **158**, 1040 (1967); C. J. Owen *et al.*, *Geophys. Res. Lett.* **23**, 1263 (1996).
28. N. F. Ness *et al.*, *J. Geophys. Res.* **73**, 3421 (1968); D. S. Colburn *et al.*, *ibid.* **76**, 2940 (1971).
29. C. T. Russell and B. R. Lichtenstein, *ibid.* **80**, 4700 (1975).
30. G. L. Siscoe and N. R. Mukherjee, *ibid.* **77**, 6042 (1972).
31. J. V. Hollweg, *ibid.* **75**, 1209 (1970).
32. C. P. Sonett and J. D. Mihalov, *ibid.* **77**, 588 (1972).
33. G. L. Siscoe *et al.*, *ibid.* **74**, 59 (1969).
34. P. Dyal *et al.*, *Nature* **236**, 381 (1972); P. Dyal *et al.*, *Proc. Lunar Sci. Conf.* **4**, 2925 (1973).
35. Apollo-like compressions would peak near 78°S latitude in Fig. 1.
36. D. H. Fairfield, *J. Geophys. Res.* **79**, 1368 (1974); M. Hoppe and C. T. Russell, *Nature* **287**, 417 (1980).
37. The contributions of P. Turin, R. Ulrich, R. Sterling, and J. Scheifele to the development of the experiment and data processing system are gratefully acknowledged. D.L.M. acknowledges discussions with S. D. Bale. WIND data were obtained from the Solar Wind Experiment (K. W. Olgilvie) and Magnetic Fields Investigation (R. P. Lepping) key parameter files. Research at the University of California, Berkeley, was supported by NASA through subcontract LMSC-HG80E477OR from Lockheed-Martin.

13 July 1998; accepted 10 August 1998

Global Elemental Maps of the Moon: The Lunar Prospector Gamma-Ray Spectrometer

D. J. Lawrence*, W. C. Feldman, B. L. Barraclough, A. B. Binder, R. C. Elphic, S. Maurice, D. R. Thomsen

Lunar Prospector gamma-ray spectrometer spectra along with counting rate maps of thorium, potassium, and iron delineate large compositional variations over the lunar surface. Thorium and potassium are highly concentrated in and around the nearside western maria and less so in the South Pole–Aitken basin. Counting rate maps of iron gamma-rays show a surface iron distribution that is in general agreement with other measurements from Clementine and the Lunar Prospector neutron detectors.

The Lunar Prospector (LP) gamma-ray spectrometer (GRS) has acquired global maps of elemental composition of the moon. It has long been known that such maps will significantly improve our understanding of lunar formation and evolution (*1*). For example, one long-standing issue of lunar formation concerns the bulk composition of the moon. There are suggestions from Apollo, Galileo, and Clementine data that the moon is enriched in refractory elements (Al, U, and Th) and FeO compared to Earth (*2*). If so, then lunar origin models that assume that most of the moon's material comes from Earth's mantle would not be correct. Another question is the compositional variability and evolution of the lunar highlands, which contain KREEP-rich materials [potassium (K), rare earth elements (REE), and phosphorus (P)]. KREEP-rich rocks are thought to have formed at the lunar crust-mantle boundary as the final product of the initial differentiation of the moon. The distribution of these rocks on the lunar surface therefore gives information about how the lunar crust has evolved over time. Other issues that can be addressed in the future using GRS data include: (i) identifying and delineating basaltic units in the maria; (ii) determining the composition of ancient or "cryptic" mare units found in the highlands using Clementine data (*3*), and searching for more of these units using mainly the Fe and Ti data; (iii) identifying and

D. J. Lawrence, W. C. Feldman, B. L. Barraclough, R. C. Elphic, D. R. Thomsen, Space and Atmospheric Sciences, Mail Stop D466, Los Alamos National Laboratory, Los Alamos, NM 87545, USA. Telephone: 505-667-0945, Fax: 505-665-7395, e-mail: djlawrence@lanl.gov. A. B. Binder, Lunar Research Institute, Gilroy, CA, 95020, USA. S. Maurice, Observatoire Midi-Pyrénées, Toulouse, France.

*To whom correspondence should be addressed.

delineating highland petrologic units; and (iv) searching for anomalous areas with unusual elemental compositions that might be indicative of deposits with resource potential.

Gamma-ray spectra. Here we present spectra (Fig. 1) measured from 16 January to 16 June, 1998. During these 150 days, 5% of the data were lost because of either incomplete coverage from the Deep Space Network, bad sync words, or bad check sums in the GRS data frames. Another 7% of the data were not used because of high backgrounds associated with solar energetic particle events that occurred from 20 April to 10 May. Our accepted data set contains a total of 132 days of data, or 356,691 separate 32-s gamma-ray spectra. The average number of spectra per 5° by 5° selenographic latitude-longitude pixel at the equator is 140, which is equivalent to 74 minutes of integration time (the GRS footpoint is around 150 by 150 km, or 5° by 5° at the equator). Because LP is in a polar orbit, the integration time scales as 1/cos(latitude), so that integration times for equivalent areas in the polar regions are substantially larger. This 5-month data set represents less than half of the total data that will be gathered during the prime mission. For comparison, the combined Apollo 15 and 16 GRS data set contained only 12.6 min per 5° × 5° selenographic latitude/longitude pixel at the equator (*4*).

The spectra of Fig. 1 were created by subtracting approximately three times the rejected GRS spectra from the accepted GRS spectra (*5, 6*). Laboratory calibrations done before launch show that this procedure reduces the background from gamma-ray escape peaks that are 0.511 MeV below the full-energy peaks and continuum gamma-rays that have Compton scattered in either the bismuth germanate (BGO) crystal of the GRS or in the lunar surface (*5*). Gain, dead time, and cosmic ray corrections have also been made to the data. The magnitude of the gain variations ranged from 0 to 0.5% over 12 hours. The average deadtime was about 4 to 4.5% and it slowly varied along the orbit from 3.5% to 5%. The correction for the cosmic ray flux variations was made by normalizing the data to the count rate of gamma-rays between 8 to 8.75 MeV. Because many of these higher energy gamma-rays are produced by processes other than the de-excitation of nuclei (for example, π^0 decay from cosmic rays hitting the moon's surface), they have little dependence on lunar composition. The 8 to 8.75 MeV gamma-ray counting rate therefore represents the baseline gamma-ray production from the moon that varies according to the flux of galactic cosmic rays.

Qualitatively, all three spectra in Fig. 1 have similar features. The general shape of the background appears to be a double exponential with a breakpoint around 4 MeV. Full energy peaks are also seen for a number of elements in the LP GRS spectra. For the energy resolution of the GRS (*7*) all of these peaks have contributions from two or more elements. Yet, for some elements, such as Fe, O, Th, Si, and K, the dominant contribution is from a single element. In contrast, other peaks are present that have comparable contributions from two or more elements. For example, both Ti and O have gamma-ray lines with similar fluxes at or near 7.0 MeV. The line at 2.2 MeV is due to aluminum and uranium gamma-rays coming from the lunar surface and gamma-rays coming from the hydrogen-neutron capture reaction in the graphite epoxy of the GRS housing. Because the mass of the housing and the neutron flux are known, the contamination in the 2.2 MeV line from the H-n capture reaction can eventually be accounted for to provide an estimate of the lunar aluminum and uranium composition. Below 1.4 MeV, there is a complicated structure of lines resulting mainly from U, Th, Fe, and Al (*8*).

Possible lines at 3.4 and 5.2 MeV have not yet been identified. Neither of these lines show any substantial variation over the lunar surface, so they might be due to energetic charged particle activation in the BGO crystal. Some recent studies suggest there is a Bi activation line in BGO at 3.4 MeV as a result of high-energy protons (*9*). The 5.2 MeV line, however, appears to have an energy that is too high to be an activation product.

The spectra from the Imbrium and Joule regions of the moon show that the abundances of the incompatible elements Th and K have considerable regional variations. Within the Imbrium region, there is a strong thorium peak at 2.6 MeV. In contrast, this peak is almost absent in the spectrum measured at Joule. Similar Imbrium enhancements are seen for gamma-rays less than 2 MeV, which have dominant contributions from potassium (1.46 MeV), uranium (0.6 MeV, 1.2 MeV, and 1.77 MeV), and thorium (0.6 and 0.95 MeV).

The counting rates for higher energy gamma-rays also show noticeable differences. Although the statistics for the 7.6 MeV iron gamma-ray lines are limited because the counting rate is less than 0.5 counts per 32 s, Mare Imbrium shows a higher iron abundance than does the Joule region. Near 7.0 MeV, the two regions also have differences. Most of the counts in this peak are due to oxygen (6.9 and 7.1 MeV) and titanium (6.8 MeV). Because oxygen abundance shows little variation over the lunar surface, the increase in counts seen for Imbrium near 6.8 MeV likely reflects an increased titanium abundance. The non-varying oxygen abundance is demonstrated by the oxygen-dominated lines at 4.4 MeV and 6.13 MeV, which have almost the same counting rate for both

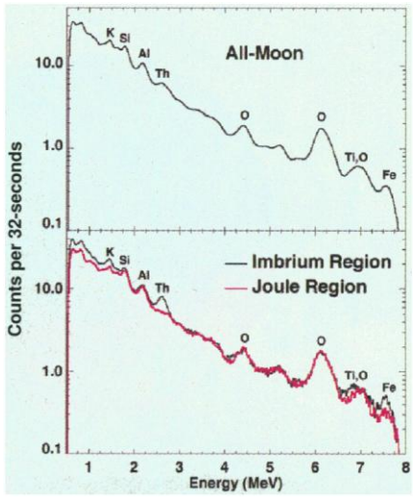

Fig. 1. LP gamma-ray spectra plotted as number of counts per 32 s versus energy. The top panel shows an average of all 356,691 gamma-ray spectra collected during the first 5 months of the mission. Because more spectra have been taken at the lunar poles, the counts in the all-moon spectrum are weighted toward the poles. The bottom panel shows spectra taken for two different lunar regions. The plot for the Imbrium Region is the average of 2694 spectra taken from 30°W to 10°W and 20°N to 40°N within Mare Imbrium. This region is known for being rich in basalts and KREEP-rich material. The plot labeled Joule Region is the average of 2677 spectra taken from 150°W to 130°W and 15°N to 30°N. The Joule crater (located at 145°W, 25°N) is located in the lunar highlands which are mainly anorthositic.

regions. Oxygen abundance is nearly constant over the moon, varying from 41% to 46% by weight (*10*).

Counting rate maps of thorium and potassium. Converting GRS counts into absolute abundances for all the measurable elements requires a series of involved detector modeling and spectral fitting procedures that have not yet been carried out. However, the elements thorium and potassium (and to a lesser extent, iron) have large compositional variations over the lunar surface as well as strong, isolated peaks in the GRS spectra. It is therefore possible to derive useful (although limited) information from maps of gamma-ray counting rates for these elements without having to compute detailed detector models or spectral fits.

The maps of Figs. 2, 3, and 4 were created using the following procedure. First, all the spectra were corrected for gain, dead time, and cosmic ray variations as a function of time. Next, the accepted GRS spectra were averaged into 5° by 5° latitude/longitude bins and counts were summed within energy bands around the central gamma-ray peaks: for thorium, the energy band was 2.4 to 2.8 MeV; for potassium the energy band was 1.3 to 1.5 MeV (*12*). The correction used to

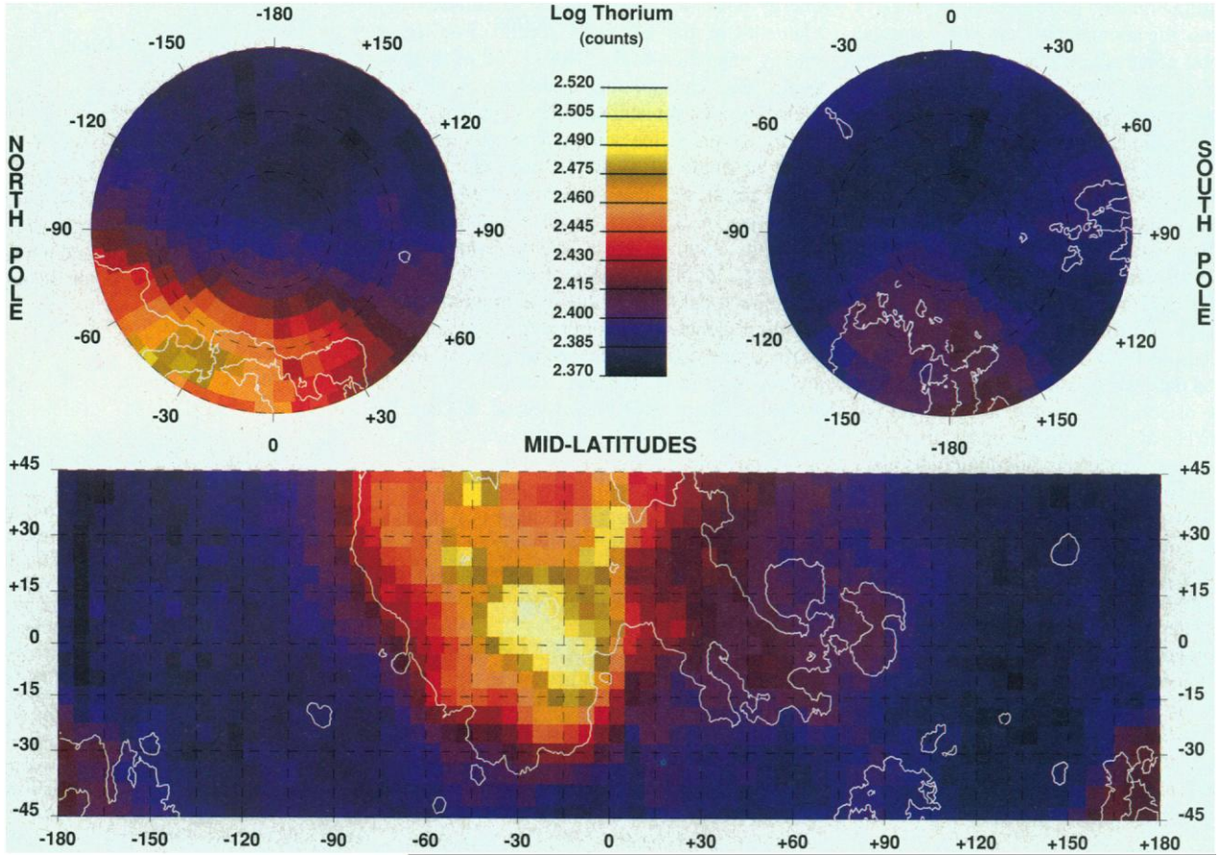
Log Thorium
(counts)
2.520
2.505
2.490
2.475
2.460
2.445
2.430
2.415
2.400
2.385
2.370
NORTH POLE
SOUTH POLE
MID-LATITUDES
-180
-150
+150
-120
+120
-90
+90
-60
+60
-30
+30
0
+45
+15
-15
-45

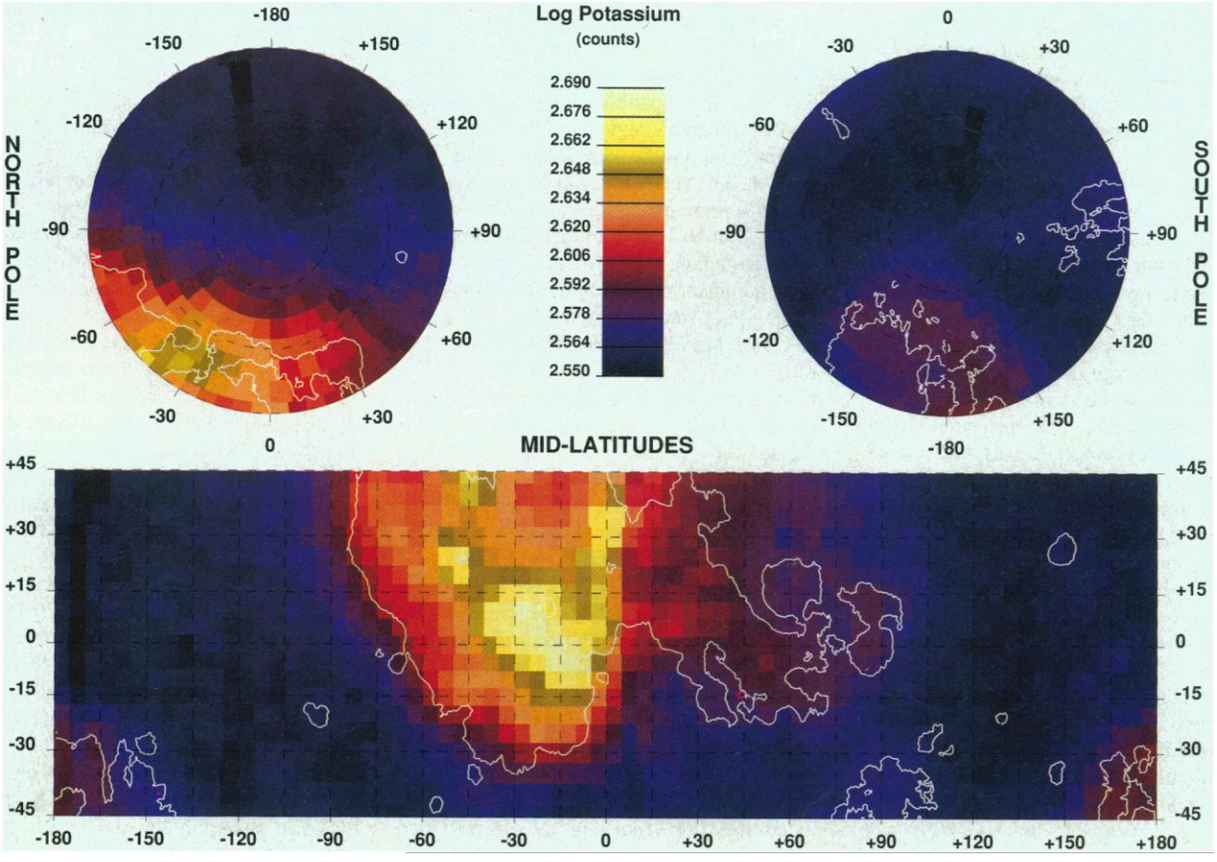
Log Potassium
(counts)
2.690
2.676
2.662
2.648
2.634
2.620
2.606
2.592
2.578
2.564
2.550
NORTH POLE
SOUTH POLE
MID-LATITUDES
-180
-150
+150
-120
+120
-90
+90
-60
+60
-30
+30
0
+45
+15
-15
-45

(*Facing page*) **Fig. 2 (top)**. Color-coded map of the log of the thorium counting rate as measured by the LP GRS. The bottom panel shows a Mercator projection for latitudes of 45°S to 45°N, and the top panel shows stereographic projections for latitudes of 45° to 90° at the north and south poles. The data are binned into equal area pixels that have a size of 5° latitude by 5° longitude at the equator. Contours of albedo data taken from Clementine data (*11*) are shown for latitudes between 70°S and 70°N. **Fig. 3 (bottom)**. Map of the log of the potassium counting rate as measured by the LP GRS. The projections and albedo contours are the same as Fig. 2.

reduce the escape peak and Compton continuum gamma-rays for the spectra of Fig. 1 was not used in this preliminary mapping analysis because the subtraction of the rejected spectra introduces too much noise into the data. Corrections that quantitatively take into account the gamma-ray escape peaks and Compton continuum will be more readily carried out once the detector modeling and spectral fitting procedures are developed.

A final correction was made to the data to account for the non-symmetric response of the GRS to gamma-rays as a function of incident angle and energy. This variation, which is of order 15%, is a smooth function of latitude and has a maximum near the south pole and a minimum near the north pole. While this variation can most accurately be taken into account by a detailed model of the detector response, in this report we used an empirical correction. Specifically, the latitude variation was characterized by a fourth degree polynomial in sin(latitude) and removed once the polynomial coefficients were known for each energy range. Once these corrections are made, it is assumed that any other variations are due to compositional variations on the moon.

These maps show that thorium and potassium are concentrated primarily on the nearside within and around the western-most maria; a secondary abundance concentration is located on the farside near Mare Ingenii in the South Pole–Aitken basin (SPA). On the nearside, the region of highest Th and K counting rates extends from the southern edge of Mare Imbrium near Copernicus to near the Apollo 14 landing site at Fra Mauro. Counts are maximum at approximately 27°W, 10°N. A region of high Th and K counting rates also surrounds the rim of Mare Imbrium. This asymmetric region is weighted with higher counts to the south of Mare Imbrium, but is also seen to extend along the Apennine mountains east of Mare Imbrium and along the highlands region north and northwest of Mare Imbrium. There is a local minimum of Th and K within Mare Imbrium located at approximately 18°W, 40°N and appears to be offset somewhat to the north of the selenographic center of Mare Imbrium at 18°W, 33°N (*13*). Most of the western mare of Oceanus Procellarum contains concentrations of Th and K that are generally enhanced although they are lower than those in the Fra Mauro and Imbrium rim regions. In contrast, the Th and K concentrations in the eastern maria (Serenitatis, Tranquillitatis, Fecunditatis, and Crisium) are much lower than the western maria; in particular, the Th and K abundances of Mare Crisium appears to be no different than its surrounding highlands.

On the farside, the highest Th and K counting rates are found in and around the SPA, but these rates are much lower than the high values on the nearside. Interestingly, the local maximum on the farside is close to the antipode of the local minimum in Mare Imbrium at approximately 165°E, 40°S (Fig. 4). While previous Apollo gamma-ray data (*4*) indicated that concentrations were enhanced in portions of the regions shown here (western Oceanus Procellarum, eastern Mare Imbrium, Fra Mauro, and Van de Graff), the LP gamma-ray data now delineate the boundaries of the Th and K enhancements and clearly indicate that these are the only lunar regions of enhanced Th and K abundances.

Many explanations have been offered regarding the distribution of KREEP-rich material on the lunar surface. Some models have stated that KREEP-rich material has been excavated from the Imbrium-Procellarum region (*14*) while others have emphasized that KREEP-rich material is of local origin and is

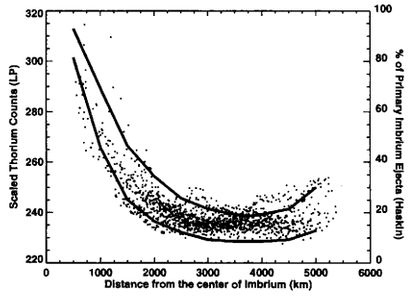

Fig. 5. The highlands thorium distribution as a function of distance from the Imbrium impact point from the LP GRS data (closed circles) and the model curves of Haskin (*14*). The highlands regions for the LP data in this figure were selected using Clementine albedo data (*11*). The upper and lower model curves are based on the largest (485 km) and smallest (335 km) estimation of the Imbrium transient crater and are calculated as the percentage of primary material ejected from Imbrium. Because the LP data are counts and not absolute abundances, the data have been slightly scaled to fall between the Haskin curves in the range of less than 1500 km.

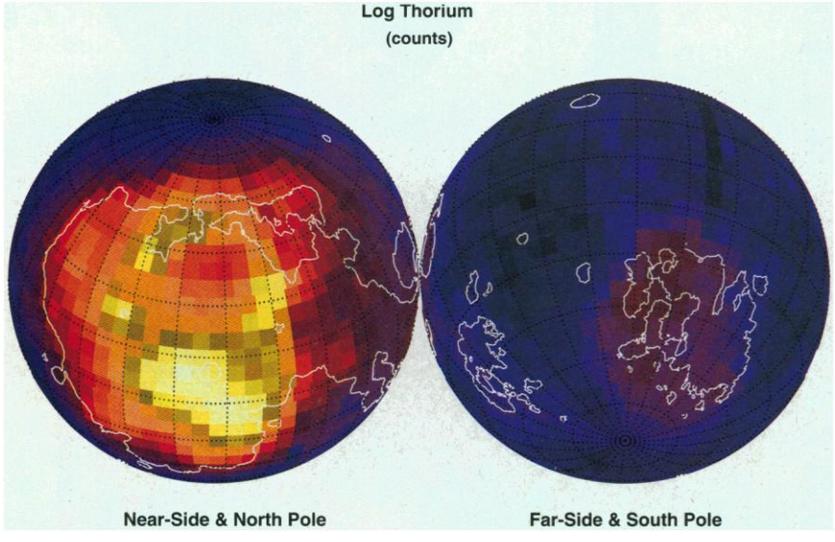

Fig. 4. Lunar nearside and farside orthographic maps of the log of the thorium counting rate. The nearside map is centered on Mare Imbrium and the farside map is centered on the antipode to Mare Imbrium. The color scale and albedo contours are the same as Fig. 2. This projection shows that the farside thorium maximum is close to the antipode of the local minimum within Mare Imbrium.

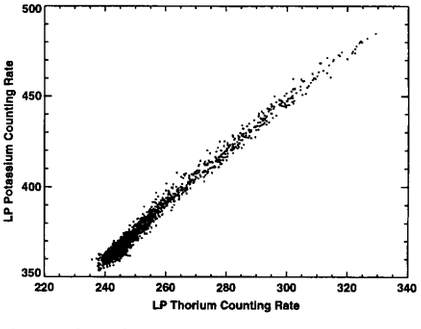

Fig. 6. Plot of potassium counting rate versus thorium counting rate as measured by the LP GRS.

produced from volcanic activity (*15*). Much work supports the idea that the distribution of KREEP-rich material involves many complexities of process and history (*15*). Because of these complexities and the limitations of the LP counting rate data, the maps presented here cannot be used to quantitatively determine the combination of mechanisms that have distributed KREEP-rich rocks over the lunar surface. However, these data may help to constrain various models. For example, Hawke and Head (*15*) have argued that most of the KREEP-rich material from Fra Mauro seems to show shock deformation effects that are incompatible with an origin as Imbrium ejecta. The highest LP counting rate in that region extends from Copernicus to Fra Mauro. This distribution appears to support this view as it is not symmetric around Mare Imbrium, but extends from the south of Imbrium to the southeast. However, the region of high Th and K around the rim of Imbrium (Fig. 4) also suggests that the some of the observed KREEP-rich material may be associated with the Imbrium impact. In the model of Haskin (*14*), it was assumed that the entire Lunar highlands Th distribution arises mainly from Imbrium impact ejecta. Fig. 5 shows the LP counting rate data for the highlands Th distribution versus distance from the Imbrium impact point, overlaid by model curves derived by Haskin. While not falling uniquely along either of the calculated KREEP distribution curves, the data are consistent with the model. Even though the Haskin model contains many assumptions and simplifications, this agreement suggests that at least some portion of the highlands KREEP distribution may be associated with the Imbrium impact.

The LP counting rate measurements are in agreement with sample measurements. Returned soil and rock samples show that thorium and potassium abundances are correlated (*16*). Both elements are incompatible in most mineral phases and so develop similar fractionation patterns. Such a correlation is also found in the LP data (Figs. 2, 3, and 6). Although this correlation is strong, the measured potassium counts may be somewhat biased from a low-level background because of overlap with Compton

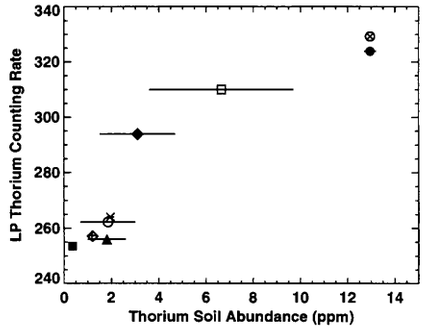

Fig. 7. Plot of measured LP thorium counting rate versus derived soil abundances in parts per million (ppm) for various landing sites. The soil measurements are taken from the data set of Korotev (*16*) who tabulated extreme high and low values for each Apollo site (no ranges were given for the Luna data because the samples were all taken from a single core). Although the symbols are plotted at the midpoint values between the extremes, they do not necessarily represent the average value for the site. The LP measurements are taken from the 150 by 150 km pixel covering each landing site. The uncertainty of the LP measurements due to counting statistics is approximately the size of the plotting symbols. The symbols for the different landing sites are as follows: ×, Apollo 11; □, Apollo 12; ●, Apollo 14; ♦, Apollo 15; ▲, Apollo 16; ○, Apollo 17; +, Luna 16; ◇, Luna 20; ■, Luna 24; ⊗, maximum LP thorium counting rate.

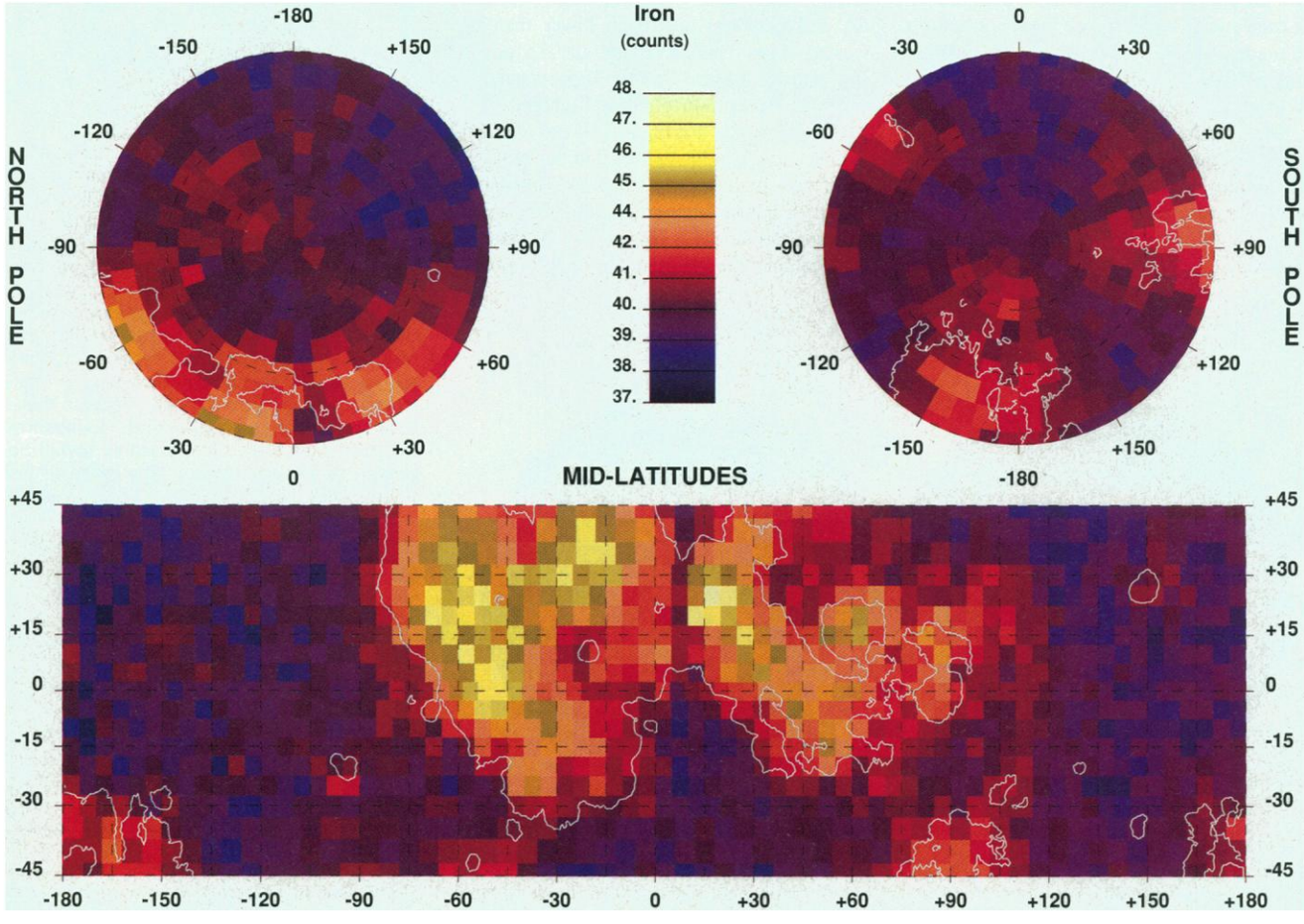

Fig. 8. Map of the iron counting rate as measured by the LP GRS. The projections and albedo contours are the same as for Figs. 2 and 3.

continuum gamma-rays produced from higher energy thorium lines.

LP thorium counting rates correspond reasonably well with Apollo and Luna thorium soil sample measurements (*16*) for most of the abundance range (Fig. 7). However, there are some discrepancies between the LP GRS measurements and sample measurements as neither the Apollo 12 (open square), Apollo 15 (closed diamond) or Apollo 14 (closed circle) data fall uniquely on a straight line with the remaining data. It is probable that the discrepancies result because the Apollo sample measurements simply do not provide an accurate measure of composition for the 150-km-radius footpoint seen by the LP GRS. However, even if Th is locally enhanced (at the Apollo 14 site, for example), the GRS measurements average out these enhancements over ~150 km. As shown in Fig. 7, the maximum thorium counting rate (located approximately 500 km from the Apollo 14 landing site) is only 3% greater than the Apollo 14 counting rate. Thus any localized thorium enhancements, if they exist, have been averaged out.

Counting rate map for 7.6-MeV gamma-rays. The statistics for the counting rate of the 7.6-MeV gamma-rays dominated by iron are not as high as for thorium and potassium. Furthermore, overlap from a 7.72-MeV aluminum line cannot yet be separated from the 7.6-MeV iron lines. Nevertheless, the available data (Figs. 1 and 8) show that the counts around 7.6 MeV vary substantially between the lunar maria and highlands regions.

The global distribution of iron inferred from the GRS data (Fig. 8) is comparable to that obtained by both the LP thermal and fast neutron detector (*17*) and earlier Clementine data (*18*). For example, high iron abundances are seen in the nearside mare, the SPA, and Mare Australe. However, we also see high gamma-ray counting rates in regions that do not appear to correlate with the high iron regions from the Clementine data, for example, east of Mare Serenitatis and Mare Frigoris. Although the LP neutron data also suggest there are high iron abundances in these regions, there are some regions of high gamma-ray counting rates on the lunar farside (for example, 90°W to 165°W and 45°N to 85°N) that do not correlate with high iron regions in either the neutron data or the Clementine data. Most of these regions are lunar highlands thought to have relatively high aluminum abundance and relatively low iron abundance. Because the 7.72-MeV aluminum gamma-ray line is the most intense of the few gamma-ray lines that can produce an interference with the 7.6-MeV iron lines (*8*), these data suggest that some of the anomalous high count rate regions may be due to elevated aluminum abundances.

References and Notes

1. The NASA Lunar Exploration Science Working Group (LExSWG), *A Planetary Science Strategy for the Moon*, JSC-25920 (1992).
2. S. R. Taylor and T. M. Esat, *Earth Processes: Reading the Isotopic Code* (*Geophys. Monogr. 95*, American Geophysical Union, Washington, DC, 1996), pp. 33–46.
3. P. H. Schultz and P. D. Spudis, *Proc. Lunar Planet. Sci. Conf.* **10**, 2899 (1979); *Nature*, **302**, 233, (1983).
4. A. E. Metzger, in *Remote Geochemical Analysis: Elemental and Mineralogical Composition*, C. M. Pieters and P. A. J. Englert, Eds. (Cambridge Univ. Press, Cambridge, 1993), pp. 341–363.
5. W. C. Feldman *et al.*, *Proc. Lunar Planet. Sci. Conf.* **27**, 355 (1996); W. C. Feldman *et al.*, *Nucl. Instrum. Methods Phys. Res. A*, in press.
6. Events triggering only by the bismuth germanate (BGO) crystal of the GRS are accepted gamma-ray events; events triggering both by the BGO and anticoincidence shield (ACS) are rejected and are due to energetic charged particles and gamma-rays that deposit a fraction of their energy in the ACS (*5*).
7. The LP GRS has an energy (E) resolution of 10.5% at 0.662 MeV and scales as $E^{-1/2}$ (*5*).
8. R. C. Reedy, *Proc. Lunar Planet. Sci. Conf.* **9**, 2961 (1978).
9. P. R. Truscott *et al.*, *IEEE Trans. Nucl. Sci.* **42**, No. 4, 946, (1995); P. R. Truscott, *ibid.* **43**, No. 3, 1510 (1996).
10. L. Haskin and P. Warren, in *Lunar Sourcebook, A User's Guide to the Moon*, G. H. Heiken, D. T. Vaniman, B. M. French, Eds. (Cambridge Univ. Press, Cambridge, 1991), pp. 357–474.
11. D. E. Smith, M. T. Zuber, G. A. Neumann, F. G. Lemoine, *J. Geophys. Res.* **102**, 1591 (1997); P. G. Lucey, P. D. Spudis, M. Zuber, D. Smith, E. Malaret, *Science* **266**, 1855 (1995).
12. The channel to energy calibration of the GRS is 0.018 MeV per channel. The energy bands being summed therefore consist of 22 channels for thorium and 11 channels for potassium.
13. F. Hörz, R. Grieve, G. Heiken, P. Spudis, A. Binder, in (*10*), pp. 61–120.
14. L. A. Haskin, *J. Geophys. Res.* **103**, 1679 (1998).
15. B. Ray Hawke and J. W. Head, *Proc. Lunar Planet. Sci. Conf.* **9**, 3285 (1978); P. D. Spudis, *ibid*, p. 3379.
16. R. L. Korotev, *J. Geophys. Res.* **103**, 1691 (1998).
17. W. C. Feldman *et al.*, *Science* **28**, 1489 (1998); R. C. Elphic *et al.*, *ibid.*, p. 1493.
18. P. G. Lucey, D. T. Blewett, B. R. Hawke, *J. Geophys. Res.* **103**, 3679 (1998).

19. We thank R. C. Reedy for helpful comments regarding this manuscript and we thank P. D. Spudis and another referee for their detailed comments. This work was supported in part by Lockheed-Martin and conducted under the auspices of the U.S. Department of Energy.

13 July 1998; accepted 11 August 1998

Major Compositional Units of the Moon: Lunar Prospector Thermal and Fast Neutrons

W. C. Feldman,* B. L. Barraclough, S. Maurice, R. C. Elphic, D. J. Lawrence, D. R. Thomsen, A. B. Binder

Global maps of thermal and fast neutron fluxes from the moon suggest three end-member compositional units. A high thermal and low fast neutron flux unit correlates with the lunar highlands and is consistent with feldspathic rocks. The South Pole–Aitken basin and a strip that surrounds the nearside maria have intermediate thermal and fast neutron flux levels, consistent with more mafic rocks. There appears to be a smooth transition between the most mafic and feldspathic compositions, which correspond to low and high surface altitudes, respectively. The maria show low thermal and high fast neutron fluxes, consistent with basaltic rocks.

Neutrons are generated by interactions between galactic cosmic rays and surface material in all planetary bodies that have sufficiently thin atmospheres. Subsequent interactions of the neutrons with surrounding material produce a steady-state, equilibrium energy spectrum that spans from the fast neutron range, where neutrons are born (energies, E, greater than several hundred thousand electron volts), to the thermal energy range ($E < 0.3$ eV), where neutrons are absorbed. Neutron energy spectra are therefore expected to reflect the composition of near-surface planetary layers. Simulations of equilibrium spectra indicate that the fast neutrons provide information primarily about the Fe and Ti content of soils (*1–3*). Epithermal neutrons (energies between ~0.3 eV and several hundred thousand electron volts) reflect primarily the abundance of hydrogen (*4*), and thermal neutrons reflect the abundance of neutron-absorbing nuclei, primarily Fe, Ti, K, Gd, and Sm (*4–7*).

The Lunar Prospector (LP) neutron spectrometer (NS) measures the flux of thermal, epithermal, and fast neutrons. Thermal and epithermal neutrons are measured using two ^{3}He-filled gas proportional counters and associated electronics (*8*). One of the counters is covered with a 0.63-mm-thick sheet of Cd, which, because of its high (>10,000 barns)

W. C. Feldman, B. L. Barraclough, R. C. Elphic, D. J. Lawrence, D. R. Thomsen, Los Alamos National Laboratory, MS D-466, Los Alamos NM 87545, USA. S. Maurice, Observatoire Midi-Pyrenees, 14 avenue Ed Belin, 31400 Toulouse, France. A. B. Binder, Lunar Research Institute, 1180 Sunrise Drive, Gilroy, CA 95020, USA.

*To whom correspondence should be addressed. E-mail: wfeldman@lanl.gov